

DOFA-CLIP: Multimodal Vision–Language Foundation Models for Earth Observation

Zhitong Xiong¹ Yi Wang¹ Weikang Yu^{1,2} Adam J Stewart¹ Jie Zhao¹
 Nils Lehmann¹ Thomas Dujardin¹ Zhenghang Yuan¹ Pedram Ghamisi²
 Xiao Xiang Zhu^{1*}

¹ Technical University of Munich ² Helmholtz-Zentrum Dresden-Rossendorf

{zhitong.xiong, xiaoxiang.zhu}@tum.de

Abstract

Earth observation (EO) spans a broad spectrum of modalities, including optical, radar, multispectral, and hyperspectral data, each capturing distinct environmental signals. However, current vision-language models in EO, particularly CLIP-based variants, remain confined to individual modalities, limiting generalization and scalability across diverse tasks. We present DOFA-CLIP (Dynamic-One-For-All CLIP), a unified vision-language foundation model that dynamically adapts to EO modalities with flexible spectral configurations through a single Transformer backbone. Our approach introduces three key contributions: 1) the construction of GeoLangBind-2M, a large-scale EO image–text dataset covering six heterogeneous modalities with rich natural language descriptions; 2) a novel training strategy called VECT (Vision-models Enhanced Contrastive Text-image pretraining), which enhances the spatial awareness of CLIP features with multiple vision foundation models; and 3) a Modality-aware Knowledge Agglomeration (MaKA) module that refines feature distillation with modality-specific awareness. DOFA-CLIP achieves state-of-the-art zero-shot performance across a wide range of EO benchmarks, including unseen modalities and a diverse number of input spectral bands. Together, these contributions establish a scalable foundation for multimodal EO understanding and open new avenues for integrating heterogeneous EO data with large language models. Code and datasets will be released.

Introduction

Earth observation (EO) technologies have undergone remarkable advancement in recent years, generating vast amounts of multimodal geospatial data spanning different sensors and scales (Xia et al. 2018; Zhu et al. 2017; Xiong et al. 2024c). In response to the exponential growth of remote sensing data, researchers have proposed foundation models (Cong et al. 2022; Reed et al. 2023; Wang et al. 2024a, 2023a; Stewart et al. 2023; Hong et al. 2024) pre-trained on large-scale EO data for multiple downstream tasks. However, these models typically focus on individual EO data modality, limiting their ability to leverage complementary characteristics across different sensor types (Zhu et al. 2024).

To address this limitation, recent works such as OFA-Net (Xiong et al. 2024b), DOFA (Xiong et al. 2024a), AnySat (Astruc et al. 2024a), OmniSat (Astruc et al. 2024b),

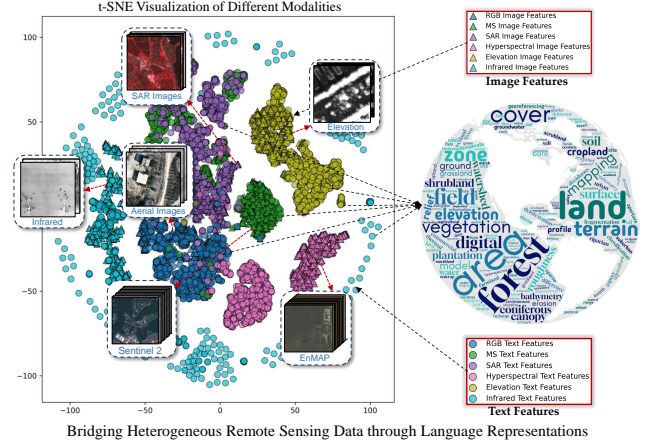


Figure 1: DOFA-CLIP employs a single unified vision Transformer to align heterogeneous EO data modalities using language as the grounding signal for cross-modal understanding and zero-shot generalization.

and FoMo-Net (Bountos, Ouaknine, and Rolnick 2023) have introduced foundation models capable of learning from multiple EO modalities within a unified framework. These approaches have demonstrated promising results in multimodal EO representation learning. However, their focus remains on unsupervised visual pretraining, lacking a structured way to align EO data with language for better interpretability and retrieval. Meanwhile, multimodal large language models like GPT (OpenAI 2023), LLaVA (Liu et al. 2023), and Pixtral (Agrawal et al. 2024) have shown remarkable capabilities in handling diverse and complex tasks. Vision-language foundation models, such as CLIP (Radford et al. 2021) and SigLIP (Zhai et al. 2023), have played a crucial role as vision encoders of such multimodal large language models. Inspired by these advances, EO-specific adaptations like RemoteCLIP (Liu et al. 2024), RS5M (Zhang et al. 2024b), RS-CLIP (Li et al. 2023), and SkyScript (Wang et al. 2024c) have attempted to bring vision-language contrastive learning to remote sensing. However, existing CLIP models for EO have limitations: 1) These models are usually limited to high-resolution RGB imagery and cannot handle modalities like multi/hyper-

spectral or SAR, which are vital for many applications. 2) Compared with vision models like DINOv2 (Oquab et al. 2023), CLIP models are unsuitable for dense understanding tasks due to the lack of spatial awareness.

Training a single powerful vision–language model capable of handling heterogeneous EO data modalities raises several core research questions (RQ). These include:

- ① **RQ1: How can we build a large-scale, semantically rich image–text dataset for diverse heterogeneous EO modalities?**
- ② **RQ2: How can we efficiently train large CLIP models for EO with better spatial awareness?**
- ③ **RQ3: How can a single CLIP model handle heterogeneous EO data while preserving modality-specific characteristics?**

To address such challenges, we propose Dynamic-One-For-All CLIP (DOFA-CLIP), a unified multimodal vision–language foundation model that aligns diverse EO modalities to the language space using a single Transformer, as shown in Fig. 1. Our contributions are as follows:

1. We introduce GeoLangBind-2M, a large-scale EO dataset comprising two million image–text pairs across six heterogeneous modalities, providing high-quality text descriptions for multimodal vision–language training.
2. We propose Vision-models Enhanced Contrastive Text-image pretraining (VECT), a simple yet effective training strategy that enhances the fine-grained spatial awareness of CLIP models with open vision foundation models.
3. We develop the Modality-aware Knowledge Agglomeration (MaKA) module to support modality-adaptive representation distillation within a unified Transformer.
4. We conduct extensive evaluations across zero-shot classification and cross-modal retrieval tasks, demonstrating state-of-the-art performance and better spatial awareness on both seen and unseen EO modalities.

Related work

Vision foundation models in Earth observation Existing pretrained models predominantly focus on RGB data, such as GFM (Mendieta et al. 2023), Scale-MAE (Reed et al. 2023), and Cross-Scale MAE (Tang et al. 2024). Others specialize in multispectral imagery, with FG-MAE (Wang et al. 2023b) and SatMAE (Cong et al. 2022) tailored for Sentinel-2 data, while SSL4EO-L (Stewart et al. 2023) is trained on Landsat imagery. SpectralGPT (Hong et al. 2024) leverages a 3D generative transformer for spectral data analysis. CROMA (Fuller, Millard, and Green 2023) and De-CUR (Wang et al. 2024b) use self-supervised multimodal learning to learn features across modalities. Satlas (Bastani et al. 2023) assembles a large-scale multi-sensor dataset, pretraining separate models for each sensor. DOFA (Xiong et al. 2024a) introduces a neural plasticity-inspired hyper-network that adapts to different sensor wavelengths, enabling joint training on five distinct sensors. OmniSat (As-truc et al. 2024b) proposes to fuse features across multiple EO modalities to learn robust multimodal representations

without labeled data. SkySense (Guo et al. 2024) utilizes separate visual encoders for different data modalities and designs a dedicated module for multimodal fusion.

Vision-language foundation models Zero-shot foundation models like CLIP (Radford et al. 2021) have significantly advanced computer vision. Building upon CLIP, SigLIP (Zhai et al. 2023) introduces a pairwise sigmoid loss function to enlarge the training batch and enhance the model performance. Zero-shot foundation models have also been investigated in EO applications. SkyScript (Wang et al. 2024c) constructs a large-scale image–text dataset by linking remote sensing images with OpenStreetMap (OpenStreetMap contributors 2017) semantics. RemoteCLIP (Liu et al. 2024) introduces an image–text dataset by generating captions from existing annotated datasets. GeoRSCLIP (Zhang et al. 2024b) introduces RS5M, an image–text dataset with 5M pairs, created by filtering existing datasets and generating captions for label-only remote sensing data. Despite these advances, existing vision–language models mainly focus on RGB data and have limitations in learning representations from multiple EO data modalities. To unify multiple data modalities, ImageBind (Girdhar et al. 2023) and TaxaBind (Sasthy et al. 2025) align multiple modalities within a shared embedding space. LanguageBind (Zhu et al. 2023) uses language as a universal intermediary for modality alignment. In the era of Large Language Models (LLMs), methods such as GeoChat (Kuckreja et al. 2024), SkyEyeGPT (Zhan, Xiong, and Yuan 2025), and TeoChat (Irvin et al. 2024) integrate CLIP-based vision models with LLMs to unify diverse tasks and achieve impressive performance.

GeoLangBind-2M Dataset

Table 1: Summary of dataset sources of GeoLangBind-2M. * indicates image–text datasets created in this work. SAR = synthetic aperture radar, MSI = multispectral imagery, HSI = hyperspectral imagery, and IR = infrared.

Image–Text Datasets	Knowledge Domain	# Samples
Seg4	General segmentation	41,172
Det10	General detection	110,800
Flair2-RGB-caption*	Land cover analysis	61,711
VRS-train	General detection	20,264
SkyScript dataset	OpenStreetMap tags	1,518,888
SAR Datasets		
MMflood-caption*	Flood mapping	6,181
SAR-ship-caption*	Ship detection	5,984
ChatEarthNet-SAR-caption*	Land cover analysis	95,620
MSI/HSI Datasets		
ChatEarthNet-S2-caption*	Land cover analysis	95,620
NLCD-hyper-caption*	Land cover analysis	15,000
Elevation Dataset		
Flair2-Elevation-caption*	Digital Elevation Model	61,711
Infrared Dataset		
IR-ship-caption*	Ships in infrared imagery	18,032
Total	—	2,050,983

In response to **RQ1**, we propose GeoLangBind-2M, a

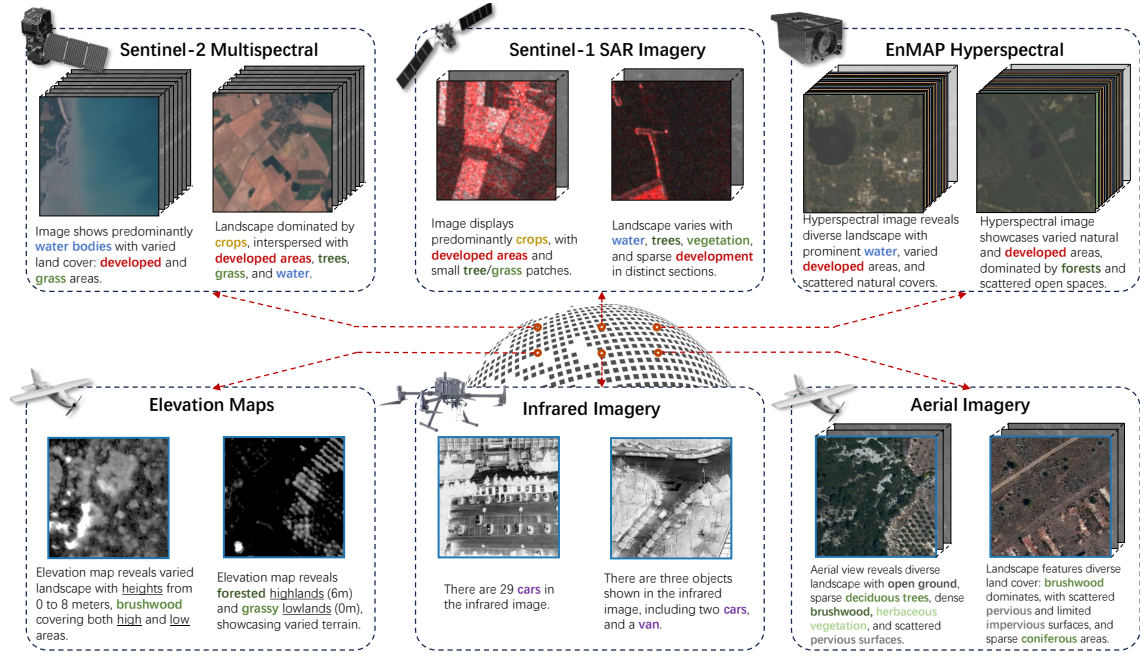


Figure 2: Visualization of data samples from GeoLangBind-2M. The dataset includes imagery from six different sensors and modalities: Sentinel-2 multispectral, Sentinel-1 SAR, EnMAP hyperspectral, elevation maps, infrared imagery, and aerial imagery. Each sample is paired with textual descriptions capturing key land cover types, objects, and geographic features.

large-scale image-text dataset covering a broad range of modalities including RGB, SAR, multispectral, hyperspectral, infrared, and elevation data, as listed in Table 1. Each image is paired with a high-quality text annotation, as illustrated in Fig. 2. All datasets are implemented using the TorchGeo library (Stewart et al. 2022). In the following, we introduce the composition of the dataset.

RGB image-text datasets High-resolution RGB images with textual descriptions form a significant portion of GeoLangBind-2M. We incorporate parts of the RemoteCLIP (Liu et al. 2024) dataset: Seg4 and Det10. We also include the training split of VRSBench (Li, Ding, and El-hoseiny 2024), which aggregates multiple object detection datasets. SkyScript (Wang et al. 2024c) is a global image-text dataset for EO, from which we include the top 30% highest quality samples. In addition to existing datasets, we construct the Flair2-RGB-caption (Garioud et al. 2023) dataset by leveraging the Pixtral-12B (Agrawal et al. 2024) model, using semantic information as prompts to generate captions for land cover features.

SAR image-text datasets To enhance the dataset with SAR-text pairs, we create MMFlood-SAR-caption (Montello, Arnaudo, and Rossi 2022), which contains captions emphasizing water extent and flooded regions (more details in supplementary material). Additionally, the SAR-ship-caption dataset includes captions describing ships in SAR images. ChatEarthNet-SAR-caption further extends the collection by covering diverse SAR scenes from Sentinel-1, focusing on land cover types.

Multispectral, hyperspectral, and elevation image-text datasets We construct ChatEarthNet-S2-caption by summarizing long, detailed descriptions from the ChatEarthNet dataset (Yuan et al. 2024). This dataset contains Sentinel-2 multispectral imagery covering more than 10 land cover types. Furthermore, we introduce NLCD-hypercaption (Braham et al. 2024), a hyperspectral dataset with 200+ EnMAP bands (Guanter et al. 2015). Like Flair2-RGB-caption, we use Pixtral-12B to generate rich captions, leveraging annotated land cover maps for enhanced descriptiveness. Similarly, we also generate captions using Pixtral-12B to construct the Flair2-Elevation-caption dataset. Further details on the construction of GeoLangBind-2M are provided in the **Supplementary materials**.

Dynamic-One-For-All CLIP

Wavelength-aware dynamic encoder

To handle the diversity of spectral bands across modalities, we adopt the dynamic encoder architecture from DOFA (Xiong et al. 2024a), as illustrated in Fig. 3. Given an input image $\mathbf{X} \in \mathbb{R}^{C \times H \times W}$ with C spectral channels, we define its corresponding central wavelengths as $\lambda \in \mathbb{R}^C$. For modalities without well-defined wavelengths, such as elevation, we assign default wavelengths equivalent to those of the RGB channels. First, a 1D sine-cosine positional encoding is applied to embed these wavelengths into a higher-dimensional space: $\mathbf{V}_\lambda = \text{PE}(\lambda) \in \mathbb{R}^{C \times d_\lambda}$, where d_λ is the embedding dimension. The encoded wavelengths \mathbf{V}_λ are then transformed using two fully-connected layers with residual connections. Next, a lightweight Trans-

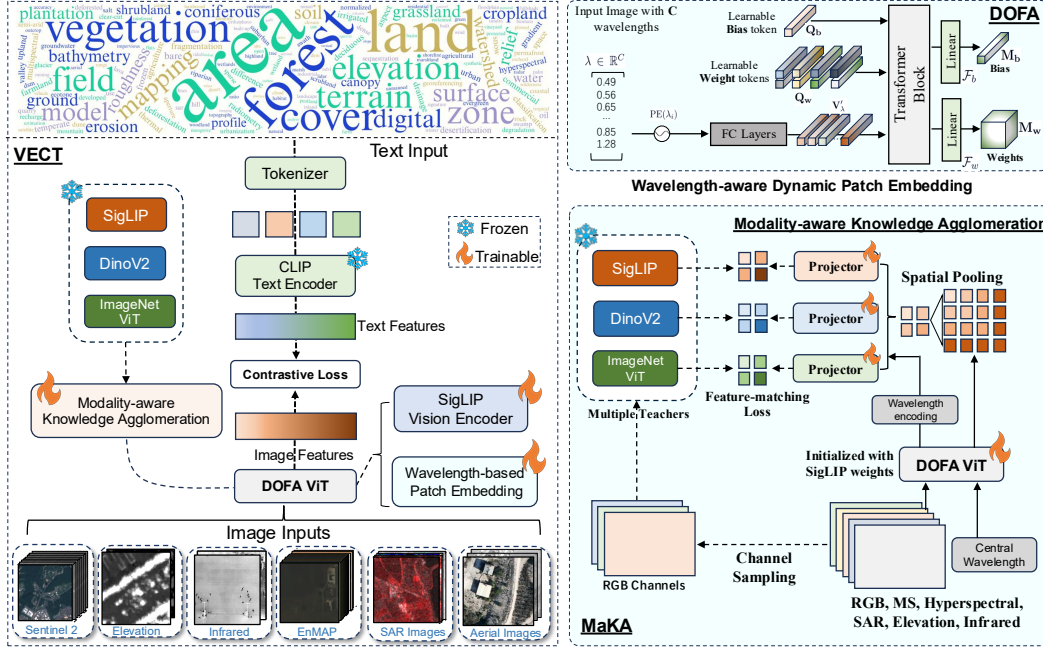


Figure 3: DOFA-CLIP aims to align diverse Earth observation data modalities into the language feature space. Vision-models Enhanced Contrastive Text-image pretraining (VECT) is proposed to enhance fine-grained image understanding. Modality-aware knowledge agglomeration (MaKA) is designed to transfer knowledge from heterogeneous sensors. The wavelength-aware dynamic patch embedding module processes multimodal images dynamically.

former (Vaswani et al. 2017) encoder processes the transformed wavelength embeddings. Specifically, we concatenate the transformed embeddings \mathbf{V}'_λ with the learnable weight query tokens \mathbf{Q}_w and a learnable bias query token \mathbf{Q}_b as input to the Transformer encoder. After the Transformer layer, the output features are passed through two fully-connected layers to generate the dynamic convolutional weights \mathbf{M}_w and biases \mathbf{M}_b . Finally, the dynamically generated weights and biases are used for patch embedding to handle EO data modalities with varying spectral channels.

Vision-models enhanced CLIP

To address RQ2, we propose VECT to enhance the spatial coherence of CLIP features by knowledge distillation from open vision models. Specifically, in addition to the contrastive loss, VECT leverages a feature-matching loss to align the intermediate features of DOFA-CLIP with features from multiple pre-trained vision models: SigLIP (Zhai et al. 2023), DINOv2 (Oquab et al. 2023), and ViT (Dosovitskiy et al. 2020). As illustrated in Fig. 3, we extract three RGB channels from multispectral or hyperspectral images as input to the teacher model. The student features $\mathbf{F}_s \in \mathbb{R}^{d_t \times H' \times W'}$ are then matched to the teacher’s features $\mathbf{F}_t \in \mathbb{R}^{d_t \times H' \times W'}$ using a combination of L_1 loss, cosine embedding loss, and mean squared error (MSE) loss:

$$L_{\text{match}} = L_{L_1}(\mathbf{F}_s, \mathbf{F}_t) + L_{\text{mse}}(\mathbf{F}_s, \mathbf{F}_t) + L_{\text{cos}}(\mathbf{F}_s, \mathbf{F}_t). \quad (1)$$

DOFA-CLIP is trained on GeoLangBind-2M using both the pairwise sigmoid loss L_{siglip} for contrastive learning and

distillation loss for feature alignment. The total loss function is:

$$L = L_{\text{siglip}} + \alpha_s L_{\text{match}}^{\text{siglip}} + \alpha_d L_{\text{match}}^{\text{dinov2}} + \alpha_v L_{\text{match}}^{\text{vit}}, \quad (2)$$

where α_s, α_d , and α_v are balancing factors for feature-matching losses of SigLIP, DINOv2, and ViT, respectively.

Modality-aware knowledge agglomeration

Considering RQ3, we introduce the modality-aware knowledge agglomeration (MaKA) module, which is used to translate DOFA-CLIP features in a modality-aware manner to facilitate effective feature matching in VECT. MaKA comprises three key components: a wavelength-aware prompt generator, a modality-aware conditional layer normalization, and a feature projector.

1. Wavelength-aware prompt generator Each modality is associated with a set of wavelengths, which we encode using a sine-cosine positional encoding function. Given input wavelengths $\lambda \in \mathbb{R}^C$, we first obtain their positional embeddings $\mathbf{V}_\lambda \in \mathbb{R}^{C \times d_\lambda}$. To generate the modality-aware prompt vector, we apply a linear projection $\mathbf{W}_{\text{proj}} \in \mathbb{R}^{d \times d_\lambda}$ to each row of \mathbf{V}_λ , then compute the mean over the C wavelengths:

$$\mathbf{V}_p = \frac{1}{C} \sum_{i=1}^C (\mathbf{W}_{\text{proj}} \mathbf{V}_{\lambda_i}), \quad (3)$$

where $\mathbf{V}_p \in \mathbb{R}^d$ is the fused modality embedding. This final embedding vector \mathbf{V}_p captures modality-specific information derived from the provided wavelengths.

2. Modality-aware layer normalization Given the feature map from the last layer of the DOFA-CLIP model, we first interpolate it to match the teacher’s feature resolution, denoted as $\mathbf{F} \in \mathbb{R}^{d \times H' \times W'}$, omitting the batch dimension for simplicity. With \mathbf{F} and a modality prompt $\mathbf{V}_p \in \mathbb{R}^d$, our goal is to perform layer normalization that dynamically adapts to the modality. To achieve this, we introduce modality-aware conditional layer normalization as follows.

First, we derive two learnable modulation vectors, $\gamma, \beta \in \mathbb{R}^d$, from the modality prompt via a linear transformation:

$$\begin{bmatrix} \gamma \\ \beta \end{bmatrix} = \mathbf{W}_{\text{prompt}} \mathbf{V}_p \in \mathbb{R}^{2d}, \quad (4)$$

where $\mathbf{W}_{\text{prompt}} \in \mathbb{R}^{2d \times d}$. We then split the output into $\gamma, \beta \in \mathbb{R}^d$ and reshape them to broadcast over the spatial dimensions:

$$\gamma \rightarrow (1, d, 1, 1), \quad \beta \rightarrow (1, d, 1, 1). \quad (5)$$

Let $\text{LN}(\mathbf{F})$ denote the standard channel-wise layer normalization of \mathbf{F} . The modality-aware layer normalization is then defined as:

$$\mathbf{F}' = \text{LN}(\mathbf{F}) + \gamma \odot \text{LN}(\mathbf{F}) + \beta, \quad (6)$$

where \odot denotes the Hadamard product. Note that we use the modality-aware layer normalization to learn the residual information specific to each modality.

3. Projector module A convolutional layer is applied to adjust the feature representation \mathbf{F}' to channel dimensions d_t of the corresponding teachers. The final representation is then used to compute the feature-matching loss for model distillation. This design ensures that the learned features are both *aligned* and *modality-specific*, enhancing robust adaptation across different input modalities.

To address the data imbalance issue, we employ a **weight space merging** strategy (Ilharco et al. 2022). Since RGB data is the most dominant modality, we split the dataset into two parts: RGB data and non-RGB data. We first train two separate DOFA-CLIP models on these subsets. Then, we merge their weights to obtain a unified model that can handle both RGB and other modalities. Since the original SigLIP model is trained on massive data, we also merge the original SigLIP weights with our model. For clarity, let θ_{siglip} be the original SigLIP model weights, θ_{rgb} be the DOFA-CLIP model weights trained on the RGB subset, θ_{others} be the DOFA-CLIP model weights trained on the other five modalities. In the first step, we merge θ_{siglip} and θ_{rgb} using a simple linear weight merging strategy:

$$\theta^* = (1 - m_1) \theta_{\text{siglip}} + m_1 \theta_{\text{rgb}}, \quad (7)$$

where m_1 controls the weighting ratio between the two models. Next, we merge the intermediate weights θ^* with θ_{others} to obtain the final model:

$$\theta = (1 - m_2) \theta^* + m_2 \theta_{\text{others}}, \quad (8)$$

where m_2 determines the contribution of the non-RGB modalities. We conduct ablation studies by varying m_1 and m_2 to search for optimal weighting ratios. While more advanced merging methods exist (Akiba et al. 2025), we use a linear approach to assess its effectiveness on heterogeneous EO data, leaving sophisticated strategies for future work.

Experiments

Implementation details

DOFA-CLIP is trained on 8 NVIDIA A100 40GB GPUs for the base model and 8 NVIDIA A100 80GB GPUs for the large version. For the base version, we use a ViT-Base architecture (patch size 16) pretrained on WebLI (Chen et al. 2022). The teacher models are ViT-Base-SigLIP (224), DINOv2-ViT-L/14, and ViT-Huge (ImageNet). The large version is based on SoViT-400m (Alabdulmohsin et al. 2023) (patch size 14, input size 384), with teacher models ViT-So400m-SigLIP (384), DINOv2-ViT-L/14, and ViT-Large (ImageNet). Training is conducted for 20 epochs using AdamW (learning rate $5e-4$, weight decay $1e-7$).

Performance comparison

We follow the evaluation protocols of Wang et al. (2024c) and evaluate the models via zero-shot classification tasks. Specifically, the following eleven image scene classification datasets are used: AID (Xia et al. 2017), EuroSAT (Helber et al. 2019), fMoW (Christie et al. 2018), Million-AID (Long et al. 2021), PatternNet (Zhou et al. 2018), NWPU-RESISC45 (Cheng, Han, and Lu 2017), RSI-CB256 (Li et al. 2017), as well as the fine-grained attribute classification datasets. In addition, we further compare these models on some datasets from the GEO-Bench suite (Lacoste et al. 2024): m-bigearthnet (Sumbul et al. 2019), m-so2sat (Zhu et al. 2019), and m-forestnet (Irvin et al. 2020).

Overall zero-shot performance As shown in Table 2, DOFA-CLIP establishes new state-of-the-art results in zero-shot remote-sensing image classification. Compared with existing CLIP-based baselines such as CLIP-original, RemoteCLIP, CLIP-laion-RS, and the various SkyCLIP configurations, DOFA-CLIP-B-224 consistently outperforms all counterparts. Its average accuracy across the eight scene datasets is significantly higher than that of the other base models. The Larger variant of DOFA-CLIP with higher resolution yields further accuracy gains. On three fine-grained roof-attribute classification tasks, both DOFA-CLIP variants achieve strong accuracy on roof shape and surface, significantly outperforming other methods. Although the results on smoothness remain more modest, our approach still provides a clear improvement over existing approaches.

Zero-shot classification on multispectral imagery The zero-shot classification results on three GEO-Bench datasets are presented in Table 3. DOFA-CLIP demonstrates competitive or superior zero-shot multi-label classification performance compared to existing models on the m-bigearthnet dataset (43 classes). For the m-so2sat dataset (17 classes), when utilizing five spectral bands, the performance decreases slightly due to the significantly less multispectral training data compared to RGB. *Note that competitive models cannot process 5-band images as input for zero-shot classification.* On the m-forestnet dataset (12 classes), DOFA-CLIP substantially outperforms other models and shows remarkable accuracy improvements when using five spectral bands as input. Notably, the m-forestnet dataset uses Landsat-8 data, which is unseen in our training dataset.

Table 2: Zero-shot comparison of various models on scene and fine-grained classification tasks. Bold values indicate the best performance.

ViT	Model	Scene classification								Fine-grained classification			
		SkyScript	AID	EuroSAT	fMoW	Million-AID	PatternNet	RESISC	RSI-CB	Avg.	Roof shape	Smoothness	Surface
Base	CLIP-original	40.16	69.55	32.11	17.62	57.27	64.09	65.71	41.26	49.66	31.50	26.80	61.36
	Human-curated captions	40.03	71.05	33.85	18.02	57.48	66.56	66.04	42.73	50.82	28.50	27.80	60.91
	RemoteCLIP	27.06	87.05	30.74	11.13	46.26	56.05	67.88	44.55	49.09	30.50	21.00	43.86
	CLIP-laion-RS	40.77	69.55	37.63	19.16	56.59	64.79	64.63	41.79	50.59	28.83	27.60	62.27
	SkyCLIP-50	52.98	70.90	33.30	19.24	62.69	72.18	66.67	46.20	53.02	26.00	38.00	67.73
Large	DOFA-CLIP-B-224	70.39	77.60	52.30	20.17	64.91	76.68	67.21	49.53	59.85	44.33	20.00	72.73
	CLIP-original	55.06	69.25	41.89	26.19	57.88	71.39	66.70	43.02	53.76	37.50	25.40	42.73
	Human-curated captions	56.09	72.95	41.96	26.33	58.47	74.86	68.70	44.60	55.41	37.00	26.60	40.00
	RemoteCLIP	34.40	70.85	27.81	16.77	47.20	61.91	74.31	50.79	49.99	34.33	34.20	55.45
	CLIP-laion-RS	58.81	71.70	54.30	27.21	60.77	72.68	71.21	48.21	57.82	40.50	37.60	53.41
	SkyCLIP-20	67.94	71.95	53.63	28.04	65.68	78.62	70.70	50.03	59.98	44.83	26.80	61.36
	SkyCLIP-30	69.08	72.15	52.44	27.77	66.40	79.67	70.77	50.19	59.99	46.17	30.80	64.32
	SkyCLIP-50	70.89	71.70	51.33	27.12	67.45	80.88	70.94	50.09	59.93	46.83	35.80	67.50
	DOFA-CLIP-L-384	76.83	75.50	59.04	29.10	70.16	80.17	73.15	51.62	64.45	61.83	26.00	81.36

Table 3: Zero-shot comparison on GeoBench datasets with non-RGB data. Bold values indicate the best performance.

Model (Base version)	m-bigearthnet			m-so2sat		m-forestnet	
	Precision	Recall	F1	RGB	Sentinel-2 (5 bands)	RGB	Landsat-8 (5 bands)
SigLIP	45.34	12.36	16.82	12.88	-	8.16	-
RemoteCLIP	33.82	20.35	18.84	10.75	-	8.46	-
SkyCLIP-50	39.91	19.58	20.32	11.97	-	10.78	-
DOFA-CLIP-B (224)	47.70	20.37	23.69	17.95	14.60	13.60	17.02

Cross-modal retrieval performance Table 4 compares DOFA-CLIP against recent methods on three benchmark caption datasets: RSICD, RSITMD, and UCM-caption. We report Recall@1, Recall@5, and Recall@10 for both image-to-text and text-to-image retrieval. Despite the inherent difficulty of remote-sensing cross-modal tasks, DOFA-CLIP-L consistently achieves competitive or higher recall scores than most competitive baselines, including CLIP-original, CLIP-laion-RS, and SkyCLIP-30.

Ablation studies

Weight merging and MaKA Table 5 presents the results of our ablation experiments, evaluating the effects of weight merging and MaKA across different models on the AID zero-shot classification dataset. The baseline SigLIP model can be significantly improved by incorporating the DOFA-CLIP-B (RGB) model, trained on the RGB part of GeoLangBind-2M. The model trained with our MaKA module (for distillation) can largely outperform the non-distilled version. DOFA-CLIP-B (Others), trained on non-RGB modalities, performs lower than its RGB counterpart. When merged with SigLIP, the performance can be significantly improved. DOFA-CLIP-B (Mixed) is the model trained with all the data modalities mixed together. When compared with the DOFA-CLIP-B (Merging), the performance is significantly lower. This demonstrates that weight merging is more effective and flexible than direct mixing of data modalities.

MaKA enhances segmentation performance As presented in Table 6, we conducted ablation studies on the MADOS (Kikaki et al. 2024), m-nz-cattle (Abuaiadah and Switzer 2022), and m-NeonTree (Weinstein et al. 2021)

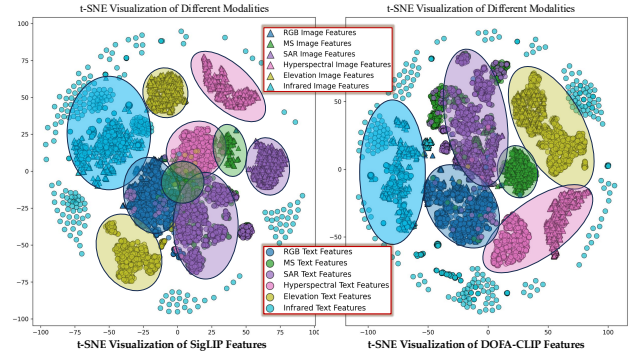


Figure 4: t-SNE visualization of feature distributions for SigLIP features (left) and DOFA-CLIP-L-384 model (right).

datasets. DOFA-CLIP-B without MaKA represents a model trained using a baseline distillation method that does not incorporate modality-specific wavelengths as conditioning. The results demonstrate the significant effectiveness of the MaKA module, showing consistent performance improvements across all datasets. **More details are in the supplementary material.**

Weight merging ratios In Table 7 and 8, a linear search is conducted to determine the optimal ratios for weight merging. Based on the results, we select 0.9 for m_1 to merge the weights of SigLIP and DOFA-CLIP (RGB). We choose 0.5 for merging weights of the intermediate weights and DOFA-CLIP (Others). Thus, we set $m_1 = 0.9$ and $m_2 = 0.5$ to derive our final model weights. *Note that the weight merging is executed a single time using a designated zero-shot*

Table 4: Recall@1, recall@5, and recall@10 for cross-modal retrieval on three benchmark datasets. Bold values indicate the best performance.

Model	RSICD						RSITMD						UCM-caption					
	Image to Text			Text to Image			Image to Text			Text to Image			Image to Text			Text to Image		
	R@1	R@5	R@10	R@1	R@5	R@10	R@1	R@5	R@10	R@1	R@5	R@10	R@1	R@5	R@10	R@1	R@5	R@10
<i>RSICD, RSITMD, and/or UCM-caption seen in training</i>																		
AMFMN (Yuan et al. 2022a)	5.39	15.08	23.40	4.90	18.28	31.44	10.63	24.78	41.81	11.51	34.69	54.87	16.67	45.71	68.57	12.86	53.24	79.43
LW-MCR-u (Yuan et al. 2021)	4.39	13.35	20.29	4.30	18.85	32.34	9.73	26.77	37.61	9.25	34.07	54.03	18.10	47.14	63.81	13.14	50.38	79.52
GaLR (Yuan et al. 2022b)	6.59	19.85	31.04	4.69	19.48	32.13	14.82	31.64	42.48	11.15	36.68	51.68	—	—	—	—	—	—
<i>RSICD, RSITMD, and/or UCM-caption not seen in training</i>																		
CLIP-original	6.59	20.68	31.75	3.62	14.28	23.63	10.18	30.31	42.04	8.31	24.96	39.03	37.62	78.10	89.52	28.12	64.99	77.19
CLIP-laion-RS	8.42	23.70	35.86	5.81	19.49	30.25	13.72	32.08	44.91	10.57	31.48	46.96	39.52	79.52	90.00	29.71	62.60	80.37
SkyCLIP-30	8.97	24.15	37.97	5.85	20.53	33.53	11.73	33.19	47.35	10.19	32.47	49.08	38.57	84.29	93.81	31.83	64.19	81.96
DOFA-CLIP-L	8.42	25.16	37.05	8.15	24.90	37.73	13.94	30.31	44.47	13.45	38.70	55.78	43.33	81.43	93.81	35.28	71.62	87.80

Table 5: Ablation experiments of models on the AID zero-shot classification dataset.

Model	Distill.	Top-1 Accuracy	Top-5 Accuracy
SigLIP	—	65.95	96.20
DOFA-CLIP-B (RGB)	✓	76.90	94.55
SigLIP+DOFA-CLIP-B (RGB)	✓	77.70	95.50
SigLIP+DOFA-CLIP-B (RGB)	✗	72.00	95.80
DOFA-CLIP-B (Others)	✓	64.70	91.95
SigLIP+DOFA-CLIP-B (Others)	✓	69.50	96.20
SigLIP+DOFA-CLIP-B (Others)	✗	66.30	91.20
DOFA-CLIP-B (Mixed) (baseline)	✓	71.60	93.65
DOFA-CLIP-B (Merging) (ours)	✓	77.60	96.65

Table 6: Ablation experiments of different distillation methods on the segmentation datasets.

Model	MADOS	m-nz-cattle	m-NeonTree
SigLIP	57.2	77.5	52.3
DOFA-CLIP-B w/o MaKA	61.7	81.5	58.1
DOFA-CLIP-B w/ MaKA	62.3	82.2	59.0

classification dataset, and held fixed across all tasks.

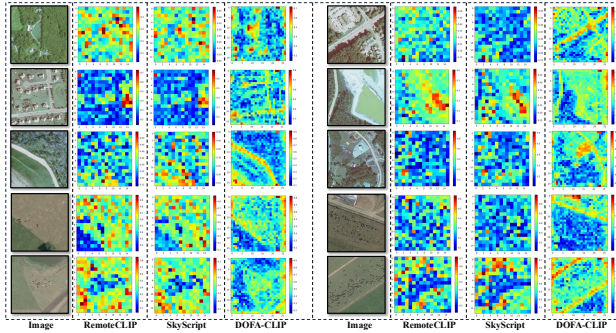


Figure 5: Visual comparison of deep features from RemoteCLIP, Skyscript, and DOFA-CLIP.

Feature visualization and analysis

On the left side of Fig. 4, we present the t-SNE plot of SigLIP features. Compared to the SigLIP features, the features of DOFA-CLIP-L-384 demonstrate a significantly

Table 7: Ratio for merging SigLIP and DOFA-CLIP-B (RGB).

m_1	AID (Top-1)	RSI-CB (Top-1)	Roof shape (Top-1)
0	65.95	38.01	41.17
0.1	44.25	27.33	37.67
0.3	56.75	31.87	38.00
0.5	74.65	41.80	44.33
0.7	77.40	45.36	53.67
0.9	77.70	47.03	57.83
1.0	76.90	46.72	58.50

Table 8: Ratio for merging weights of DOFA-CLIP-B (RGB) and DOFA-CLIP-B (Others).

m_2	AID (Top-1)	RSI-CB (Top-1)	Roof shape (Top-1)
0	77.70	47.03	57.83
0.1	78.10	47.31	57.50
0.3	78.55	47.91	55.83
0.5	78.60	49.17	52.67
0.7	76.45	49.92	52.00
0.9	76.35	43.98	63.33
1.0	69.20	34.80	59.67

stronger imagery-text alignment across all modalities, making it a powerful foundation for Earth observation tasks. In Fig. 5, we visually compare the feature heatmaps of RemoteCLIP, SkyScript, and DOFA-CLIP. DOFA-CLIP features are more spatially structured and preserve more object details, demonstrating the effectiveness of VECT.

Conclusion

We introduce DOFA-CLIP, a unified vision–language foundation model that bridges heterogeneous EO modalities through a shared language space. To achieve this, we construct GeoLangBind-2M, a large-scale image–text dataset containing six EO data modalities. DOFA-CLIP consists of a wavelength-aware encoder and a modality-aware knowledge agglomeration module to enhance fine-grained image understanding. Additionally, progressive weight merging is proposed to scale the model training to multiple data modalities. Extensive experiments demonstrate the state-of-the-art performance of DOFA-CLIP across zero-shot classification, semantic segmentation, and retrieval tasks.

Supplementary material

The supplementary material contains the following sections:

1. Details of the evaluation datasets;
2. Details on the construction of GeoLangBind-2M;
3. More visualization examples of GeoLangBind-2M;
4. Ablation studies on the distillation loss terms;
5. Confusion matrices of the zero-shot classification tasks;
6. More visualization of the features;

Details of the evaluation datasets

We evaluate DOFA-CLIP on both datasets that have been established in previous works for direct comparison, as well as additional datasets that highlight the wide-ranging capabilities of the proposed model.

The following datasets are part of the SkyScript (Wang et al. 2024c) evaluation framework, which we follow for direct comparison.

- SkyScript classification dataset (Wang et al. 2024c): contains 7,000 aerial RGB images with 70 classes and different objects than the SkyScript pretraining dataset.
- AID (Xia et al. 2017): contains 2,000 aerial RGB images and 30 image scene classes.
- EuroSAT (Helber et al. 2019): contains 27,000 Sentinel-2 images with 13 spectral bands and 10 image scene classes. We use the dedicated test split that contains 2,700 images.
- fMoW (Christie et al. 2018): contains 106,081 RGB aerial images with 62 image scene classes.
- Million-AID (Long et al. 2021): contains 10,000 RGB aerial images of varying GSD with 51 image scene classes.
- PatternNet (Zhou et al. 2018): contains 30,400 high-resolution RGB aerial images with 6–50 cm GSD and 38 image scene classes.
- NWPU-RESISC45 (Cheng, Han, and Lu 2017): contains 31,500 aerial RGB images with 0.2–30 m GSD and 45 image scene classes.
- RSI-CB (Li et al. 2017): contains 24,747 aerial RGB images and 35 image scene classes.

Additionally, we choose the GEO-Bench (Lacoste et al. 2024) suite of datasets that cover a range of relevant remote sensing tasks across different domains, sensors, and geospatial locations. Table 9 contains a detailed overview of the number of samples, sensors, and target classes in the GEO-Bench datasets.

In addition, we conduct ablation experiments on the Marine Debris and Oil Spill (MADOS) (Kikaki et al. 2024) dataset. The MADOS dataset is a high-resolution multispectral Sentinel-2 dataset for marine pollution detection. Spanning 174 globally distributed scenes (2015–2022) with 1.5M annotated pixels, it covers diverse pollutants, sea surface features, and water-related classes. Unlike existing datasets, MADOS enables scalable, generalizable deep learning models for holistic marine pollution monitoring.

FLAIR2 (RGB)



Figure 6: Word cloud for the Flair2-RGB-caption dataset.

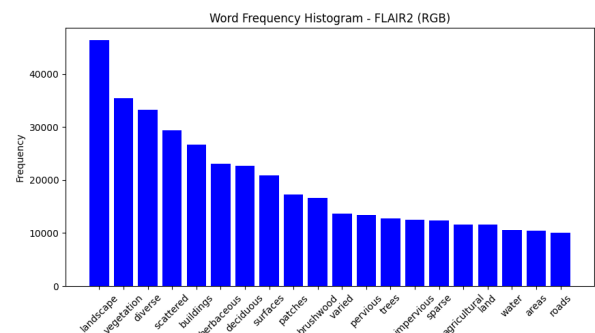


Figure 7: Word histogram for the Flair2-RGB-caption dataset.

Table 9: GEO-Bench dataset description.

Tasks	Name	Image Size	# Classes	Train	Val	Test	# Bands	Sensors
Classification	m-bigearthnet	120 x 120	43	20000	1000	1000	12	Sentinel-2
	m-so2sat	32 x 32	17	19992	986	986	18	Sentinel-2 + Sentinel-1
	m-forestnet	332 x 332	12	6464	989	993	6	Landsat-8
Segmentation	m-nz-cattle	500 x 500	2	524	66	65	3	RGB
	m-NeonTree	400 x 400	2	270	94	93	5	RGB + Hyperspectral + Elevation

Details on constructing GeoLangBind-2M

We construct our multimodal image–text dataset GeoLangBind-2M by assembling existing datasets and curating 8 new datasets. Details on the newly curated sub-datasets are as follows.

Flair2-RGB-caption For the Flair2-RGB-caption dataset, originally designed for semantic segmentation land cover classification, we employed an approach similar to the ChatEarthNet (Yuan et al. 2024) dataset construction. We select the training set of 61,711 images from FLAIR #2 (Garioud et al. 2023) and derive contextual information from their corresponding pixel-level segmentation masks. This extracted semantic content, paired with the segmentation maps as visual context, serves as the input for generating comprehensive descriptions using the Pixtral 12B (Agrawal et al. 2024) language model.

Our semantic extraction process involves calculating the distribution percentages of various terrain categories within each image and formulating these statistics into structured contextual cues. We identify all land cover categories in each segmentation map, assigning distinctive color codes to represent different semantic classes. The designed prompt explicitly defines the correspondence between color codes and land cover categories, while also incorporating the calculated percentage coverage of each land/object type within the segmentation maps. This quantitative spatial information is then processed by the Pixtral 12B model to analyze distribution patterns and generate linguistically accurate descriptions.

With this semantic framework established, we craft a prompt for generating detailed image descriptions. The prompt template variables indicated in brackets represent dynamic content populated during the semantic processing phase. The exact prompt template used for Flair2-RGB-caption creation is shown below:

You are an AI visual assistant capable of describing a scene based on a segmentation map. The map represents different land cover types using specific colors. The legend is as follows:

- [color_i] corresponds to [label_i], occupying [percent_i]% of the image.

Do not mention colors, color coding, or technical details. Use the given land cover class names exclusively. Generate a brief yet natural description of the scene by extending the sentence: “The aerial image contains [presented_labels] land types.” Provide a con-

FLAIR2 (Elevation)



Figure 8: Word cloud for the Flair2-Elevation-caption dataset.

cise summary of their spatial distribution.

In Fig. 6, we illustrate the word cloud for this dataset.

Flair2-Elevation-caption The **Flair2-Elevation-Caption** dataset is constructed to generate detailed textual descriptions of terrain characteristics by leveraging both semantic segmentation maps and elevation maps. The dataset creation follows a structured approach, similar to the Flair2-RGB-caption dataset, ensuring that the generated captions effectively describe the topographical and land cover features of each image.

To begin, we select 61,711 images from the FLAIR #2 dataset, each accompanied by a segmentation map and an elevation map. The segmentation map provides land cover information, where each pixel corresponds to a specific land class, while the elevation map encodes height values representing terrain variation. Additionally, a class label mapping is used to associate numerical class IDs with their corresponding semantic labels, such as “forest,” “urban area,” or “water body.” This combination of datasets enables a comprehensive understanding of both land cover distribution and elevation patterns.

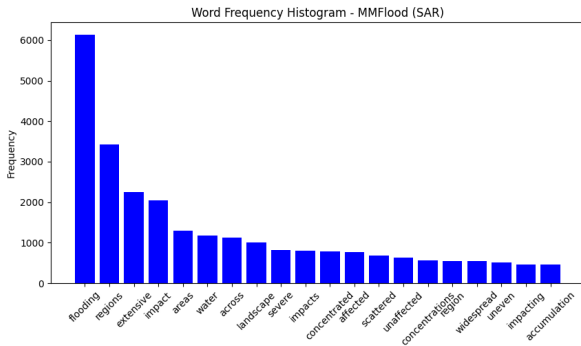


Figure 11: Word histogram for the MMflood-SAR-caption dataset.

specify their locations within the image. To ensure clarity and brevity, the generated description is limited to fewer than 70 words, making it suitable for vision-language pre-training.

The prompts are then fed into Pixtral 12B, which generates natural language captions describing each flood map. These captions, stored alongside their corresponding binary masks, form the MMFlood dataset, enabling automated flood analysis, disaster monitoring, and geospatial AI research. By combining semantic flood mapping with natural language descriptions, this dataset enhances the ability of AI models to interpret and describe flood-affected regions in a human-readable format. We also provide the word cloud in Fig. 10 to show the detailed content of this dataset. In Fig. 11, we present the histogram of the words in the MMFlood-SAR-caption dataset.

This is a flood map where areas marked with white pixels indicate flooded regions. The flooded area occupies approximately $[flood_percentage]\%$ of the entire map. Please analyze the flood map and provide insights into the affected areas.

You must generate a short description (less than 70 words) of the elevation image. First, describe the portion of floods; then introduce the location of the flooded areas.

After generating these detailed textual descriptions, we further refine the dataset by prompting Pixtral 12B to summarize each description into a concise 30-word caption. The prompts used in this summarizing process are as follows:

You are an AI assistant tasked with creating a concise 30-word caption that effectively summarizes the key points of the following content: *[caption]*

NLCD-hyper-caption The caption generation process for hyperspectral images follows a methodology similar to the FLAIR #2 dataset, ensuring consistency in semantic information extraction and description generation. Hyperspectral images provide rich spectral information across multiple wavelengths, allowing for a more detailed classification of land cover types. However, the caption generation process remains aligned with the Flair2-RGB-Caption dataset,



Figure 12: Word cloud for the NLCD-hyper-caption dataset.

differing only in the specific prompt format used to guide the Pixtral 12B model. To create captions, we first extract semantic information from the hyperspectral images using their corresponding segmentation maps. Each land cover type is identified and labeled, and its spatial distribution within the image is analyzed. Unlike conventional RGB imagery, where color-based segmentation might play a role, hyperspectral images rely on spectral signatures to differentiate land cover types, making this process crucial for accurate caption generation.

Once the land cover labels and their distributions are determined, we construct a structured prompt to generate natural language descriptions. The Pixtral 12B model is tasked with producing concise and human-readable descriptions of the scene. The prompt ensures that the generated captions focus solely on land cover types and their spatial distributions, avoiding any mention of technical details, color coding, or hyperspectral data intricacies.

Following the generation of detailed textual descriptions, we further prompt Pixtral 12B to refine the descriptions into brief and natural captions. This step ensures that the dataset provides both long-form and short-form textual annotations, improving its usability for vision-language tasks, remote sensing analysis, and multimodal learning.

The prompt template used for hyperspectral image captioning is as follows:

You are an AI visual assistant capable of describing a scene based on a segmentation map. The map represents different land cover types using specific colors. The legend is as follows:

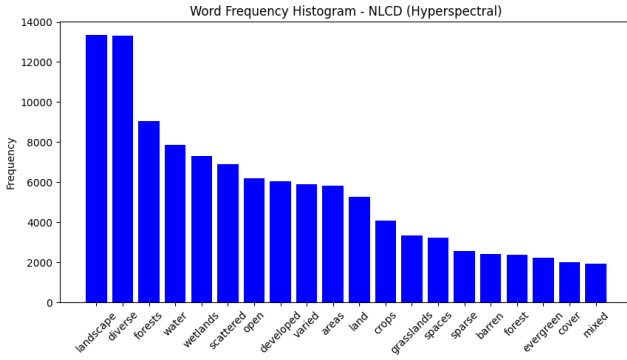


Figure 13: Word histogram for the NLCD-hyper-caption dataset.

- $[color_i]$ corresponds to $[label_i]$, occupying $[percent_i]\%$ of the image.

Do not mention any colors, color coding, or technical details. Use the given class names. Only mention land cover types in the color legend.

Generate a brief and natural description of the scene by refining: “The hyperspectral image contains $[presented_labels]$ land types.” Provide a concise description of their spatial distributions (e.g., left, right, top, bottom).

To provide a clearer overview of this dataset, we showcase the word cloud in Fig. 12. We also showcase the histogram of the words in the NLCD-hyper-caption dataset in Fig. 13.

SAR-ship-caption and IR-ship-caption For the SAR-ship-caption and IR-ship-caption subsets, we derive short captions from existing datasets to ensure high-quality textual descriptions. For IR-ship-caption, we utilize samples from the HIT-UAV dataset, specifically the data provided in Zhang et al. (2024a), which is originally designed for visual question answering tasks. To generate descriptions for infrared images, we concatenate the corresponding question and answer pairs, transforming them into concise yet informative captions.

Similarly, for the SAR-ship-caption dataset, we generate captions for SAR images using three key datasets: HRSID (Wei et al. 2020), SSDD (Zhang et al. 2021), and AIR-SARShip-2.0 (Sun, Sun, and Wang 2020). These datasets provide extensive annotated SAR imagery, enabling the creation of meaningful captions. For further details on the captioning methodology, please refer to Zhang et al. (2024a).

ChatEarthNet captions Regarding the ChatEarthNet-S2-caption and ChatEarthNet-SAR-caption datasets, we reuse the detailed descriptions provided in the original ChatEarthNet dataset. Specifically, we use Pixtral 12B (Agrawal et al. 2024) to summarize these detailed descriptions into short image captions and generate question-answer pairs for visual question answering tasks. The word cloud for ChatEarthNet-caption datasets is presented in Fig. 14. To provide more insights into the dataset, we also show the histogram in Fig. 15. The prompt is as follows:

ChatEarthNet (RGB)

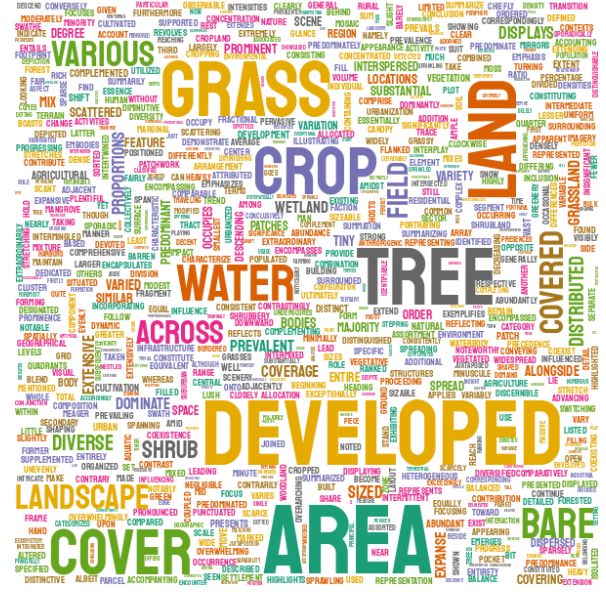


Figure 14: Word cloud for the ChatEarthNet-caption datasets.

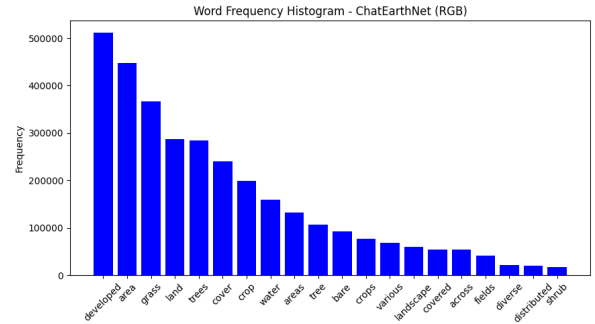


Figure 15: Word histogram for the ChatEarthNet-caption datasets.

You are an AI assistant tasked with creating a concise 30-word caption that effectively summarizes the key points of the following content: [caption]

More dataset examples

These paired samples not only capture scene-level descriptions but also highlight fine-grained properties, such as object positions and fine-grained land cover types. Thereby the dataset enables the development of *foundation models* proficient in downstream performance for land cover mapping, flood monitoring, and object detection under challenging conditions (e.g., night or cloudy weather).

In Fig. 16 and Fig. 17, we provide more examples to provide a better overview of our dataset.

Ablation studies on distillation loss terms

Table 10: Distillation loss balancing weights vs. accuracy

α_s (SigLIP)	α_d (DinoV2)	α_v (ViT)	aid (Top-1)	eurosat (Top-1)
0	0	0	59.10	32.96
1.0	0.0	0.0	61.42	33.63
1.0	1.0	0.0	65.36	35.26
1.0	1.0	1.0	68.75	38.63
2.0	0.0	0.0	64.85	33.19
2.0	0.5	0.5	64.70	25.30
2.0	1.0	1.0	69.20	36.67

Table 10 presents an ablation study on the impact of different distillation loss balancing weights (α_s , α_d , α_v) on classification accuracy for the AID and EuroSAT datasets. The baseline model (no distillation) achieves 59.10% (AID) and 32.96% (EuroSAT). Adding SigLIP distillation ($\alpha_s = 1.0$) improves performance, while combining SigLIP and DinoV2 ($\alpha_s = 1.0$, $\alpha_d = 1.0$) further enhances results, especially for AID (65.36%). Introducing ViT distillation ($\alpha_v = 1.0$) boosts EuroSAT accuracy, peaking at 38.63% when $\alpha_s = \alpha_d = \alpha_v = 1.0$. In this work, we adopt the best overall configuration, $\alpha_s = 2.0$, $\alpha_d = 1.0$, $\alpha_v = 1.0$, achieves the highest AID accuracy (69.20%) and strong EuroSAT performance (36.67%). This demonstrates the effectiveness of multi-teacher distillation.

Confusion matrices of zero-shot classification tasks

Figure 18 to Fig. 25 present the confusion matrices of our DOFA-CLIP-L-384 model on all eight datasets for zero-shot classification. These confusion matrices reveal that common model mistakes largely occur for classes that humans would also have trouble distinguishing, or for classes with similar semantic meanings. For instance, the model commonly confuses “sparse residential” and “medium residential” (RESISC45), “annual crop” and “permanent crop” (EuroSAT), “aquaculture land” and “pond” (SkyScript), “chaparral” and “desert” (RESISC45), “mine” and “quarry” (SkyScript, Million-AID), “recreational facility” and “stadium” and “playground” (fMoW, AID), and “ship” and “harbor” and “ferry terminal” (RESISC45, PatternNet).

In Fig. 26, we show the comparison of confusion matrices between SkyScript (ViT-L) and DOFA-CLIP-L-384 on fine-

grained zero-shot classification tasks. It can be clearly seen that our model performs better.

More visualization of features

To better understand the representations learned by different models, Fig. 27 visualizes the feature maps extracted from RemoteCLIP (ViT-L), SkyScript (ViT-L), and DOFA-CLIP-L-384 across two datasets: m-chesapeake and m-nz-cattle from GEO-Bench. The m-chesapeake dataset primarily focuses on land cover classification, while the m-nz-cattle dataset captures cattle in remote sensing images. The feature visualization highlights key differences in spatial structure, consistency, and detail preservation across models.

Spatially structured features DOFA-CLIP produces features with higher spatial resolution, enabling finer spatial distinctions compared to RemoteCLIP and SkyScript. The feature maps exhibit well-defined structures that align with meaningful spatial regions in the original images, such as roads, buildings, and vegetation.

Consistency across semantic classes The feature maps from DOFA-CLIP demonstrate greater consistency across images with similar semantic content. As observed, buildings and roads consistently exhibit high activations, while tree-covered areas show lower activations. This structured activation pattern is apparent across multiple samples, suggesting that DOFA-CLIP learns more stable and semantically aligned representations.

Preservation of details DOFA-CLIP retains finer details within its feature maps, capturing small-scale variations and object boundaries more effectively than the baselines. This advantage is particularly evident in the m-nz-cattle dataset, where cattle are localized with sharper feature activations, as highlighted by the red bounding boxes. RemoteCLIP and SkyScript, on the other hand, exhibit more diffused and less distinct feature responses, making object-level distinctions less precise.

References

- Abuaiadah, D.; and Switzer, A. 2022. Remote sensing dataset for detecting cows from high resolution aerial images.
- Agrawal, P.; Antoniak, S.; Hanna, E. B.; Bout, B.; Chaplot, D.; Chudnovsky, J.; Costa, D.; De Monicault, B.; Garg, S.; Gervet, T.; et al. 2024. Pixtral 12B. *arXiv preprint arXiv:2410.07073*.
- Akiba, T.; Shing, M.; Tang, Y.; Sun, Q.; and Ha, D. 2025. Evolutionary optimization of model merging recipes. *Nature Machine Intelligence*, 1–10.
- Alabdulmohsin, I. M.; Zhai, X.; Kolesnikov, A.; and Beyer, L. 2023. Getting vit in shape: Scaling laws for compute-optimal model design. *Advances in Neural Information Processing Systems*, 36: 16406–16425.
- Astruc, G.; Gonthier, N.; Mallet, C.; and Landrieu, L. 2024a. AnySat: An Earth Observation Model for Any Resolutions, Scales, and Modalities. *arXiv preprint arXiv:2412.14123*.

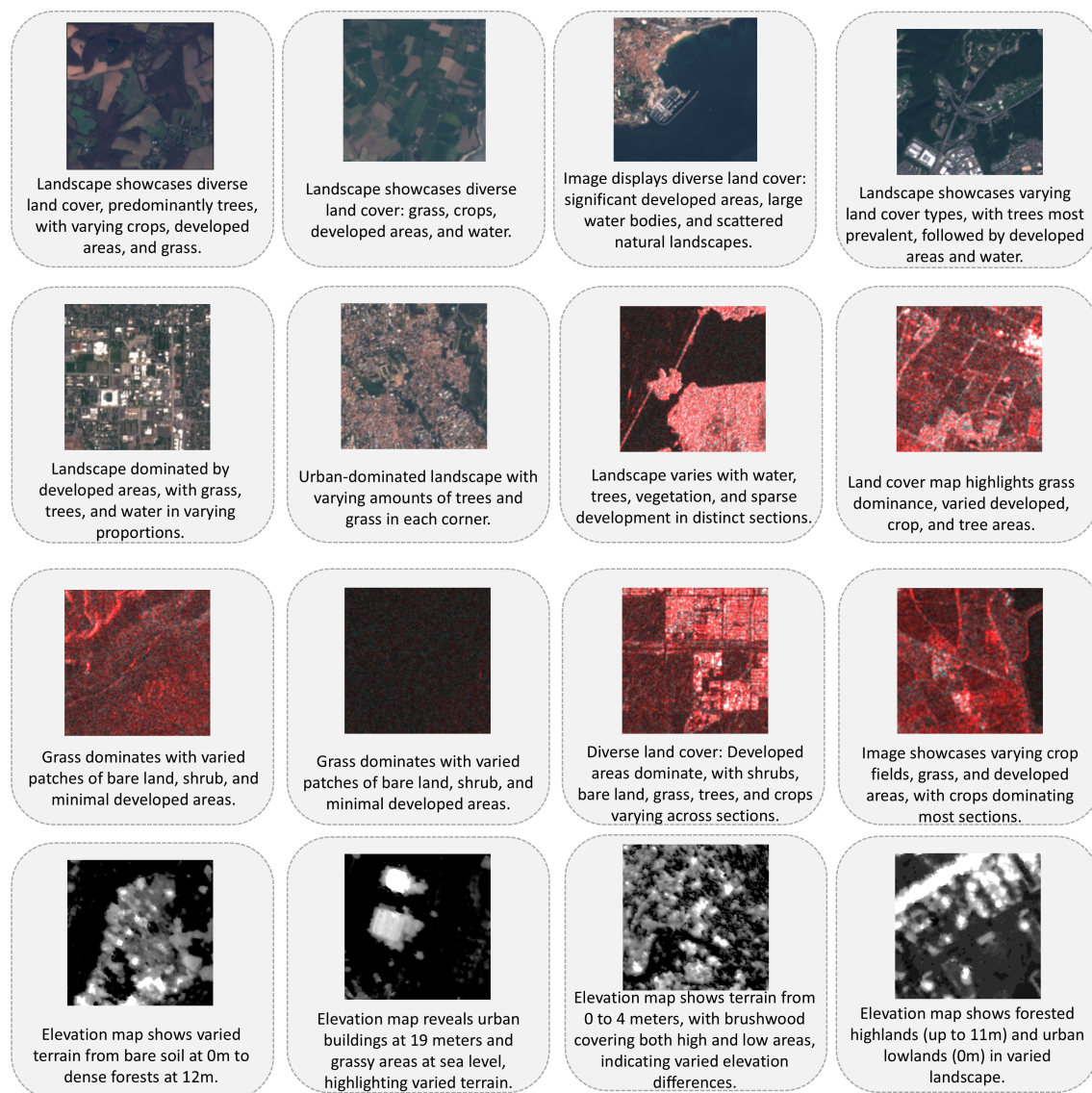


Figure 16: More examples of the image-text pair of GeoLangBind-2M, our multimodal image-text dataset.

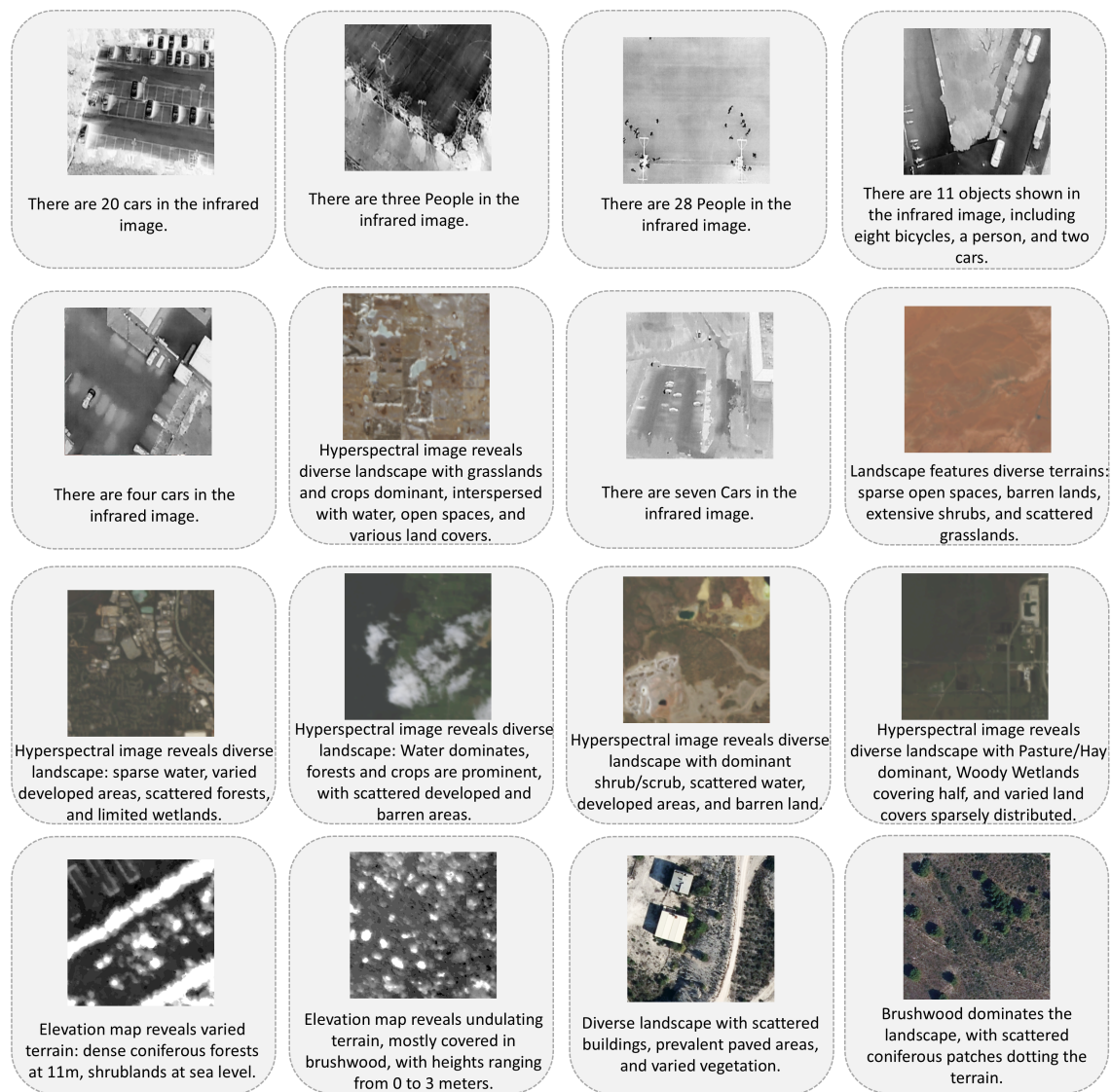


Figure 17: More examples of the image-text pair of GeoLangBind-2M, our multimodal image-text dataset.

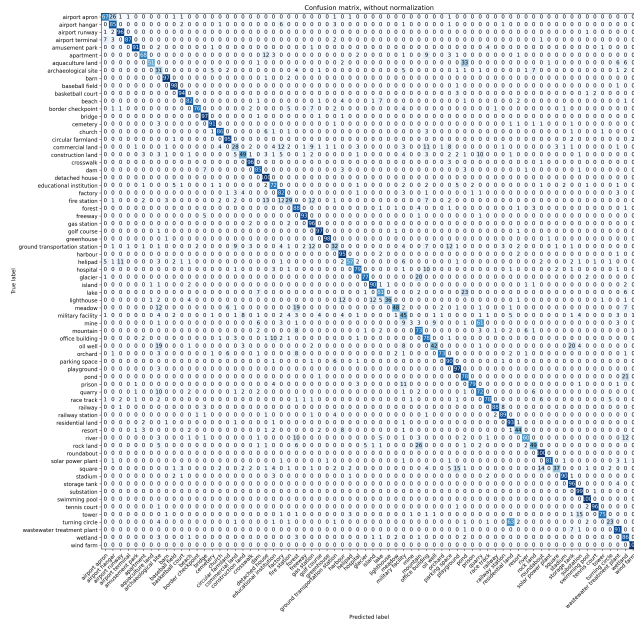


Figure 18: Confusion matrix of the zero-shot classification results of DOFA-CLIP-L-384 on SkyScript dataset.

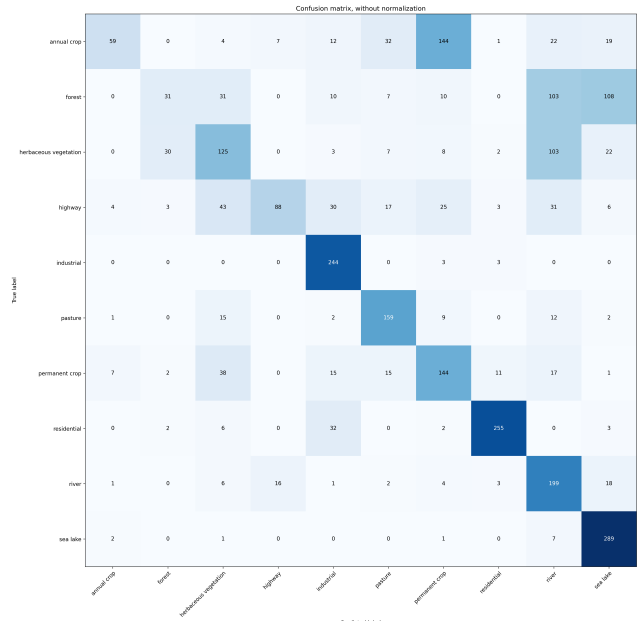


Figure 20: Confusion matrix of the zero-shot classification results of DOFA-CLIP-L-384 on EuroSAT dataset.

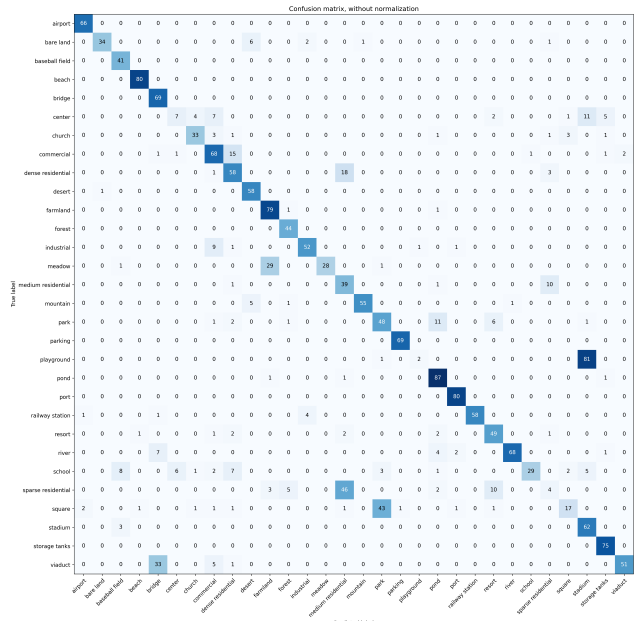


Figure 19: Confusion matrix of the zero-shot classification results of DOFA-CLIP-L-384 on AID dataset.

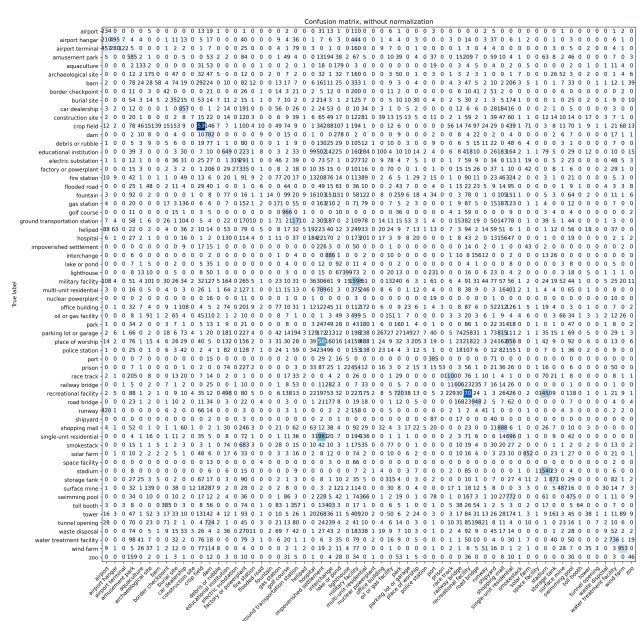


Figure 21: Confusion matrix of the zero-shot classification results of DOFA-CLIP-L-384 on fMoW dataset.

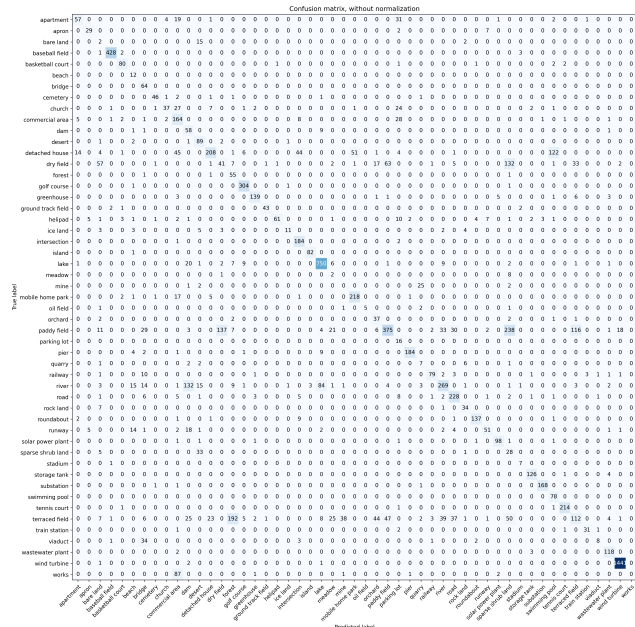


Figure 22: Confusion matrix of the zero-shot classification results of DOFA-CLIP-L-384 on Million-AID dataset.

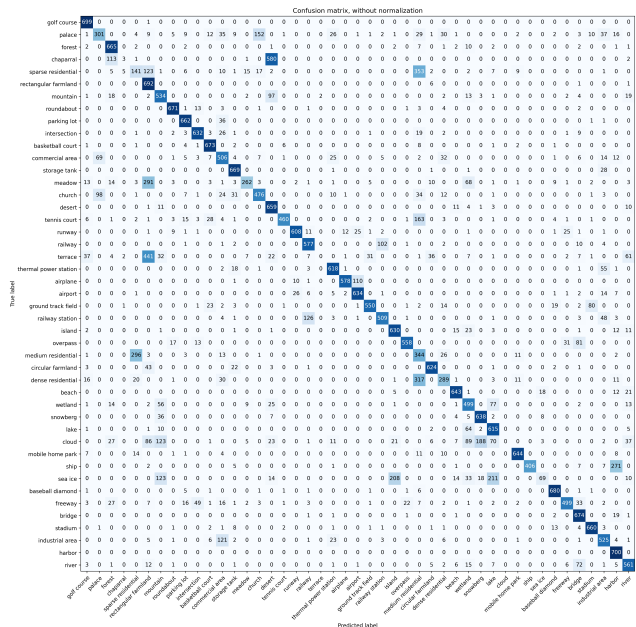


Figure 24: Confusion matrix of the zero-shot classification results of DOFA-CLIP-L-384 on the RESISC45 dataset.

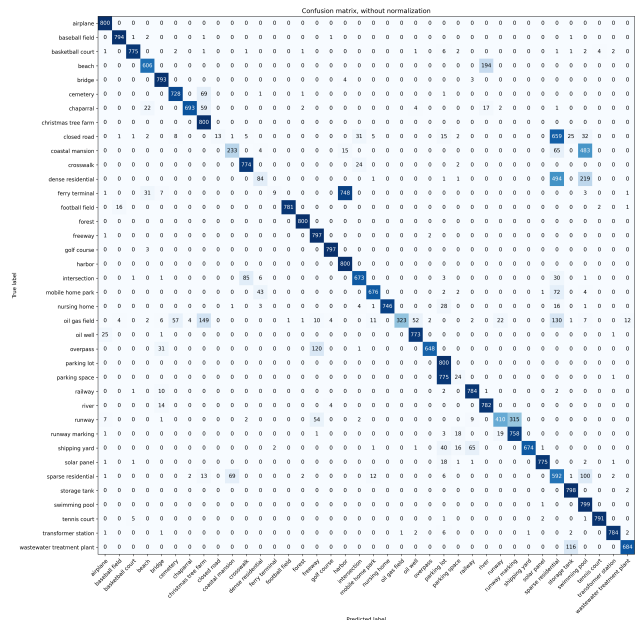


Figure 23: Confusion matrix of the zero-shot classification results of DOFA-CLIP-L-384 on PatternNet dataset.

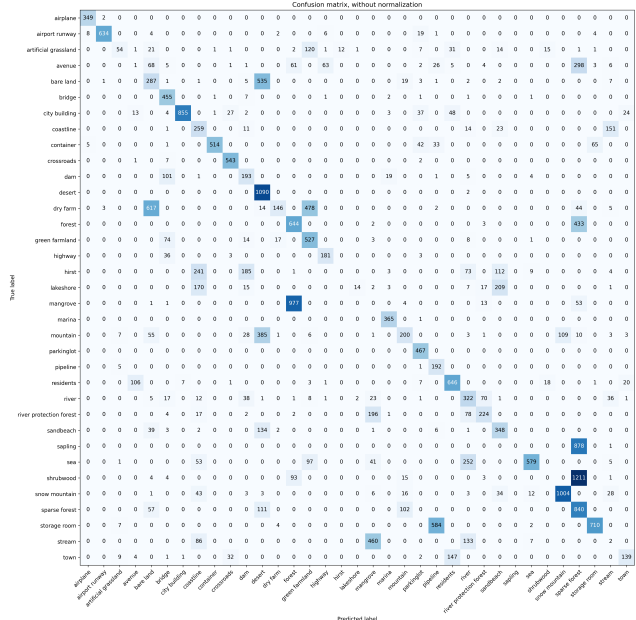
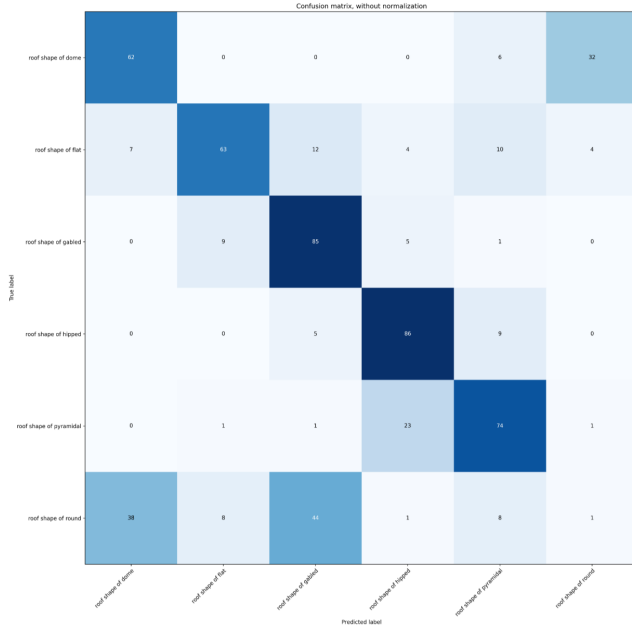
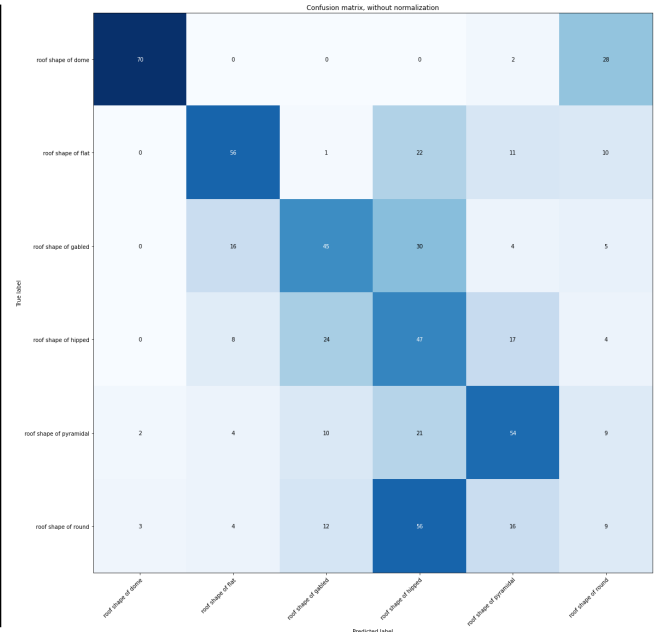


Figure 25: Confusion matrix of the zero-shot classification results of DOFA-CLIP-L-384 on RSICB dataset.



Zero-shot Fine-grained Classification Results of GeoLangBind



Zero-shot Fine-grained Classification Results of SkyScript

Figure 26: Comparison of confusion matrices between SkyScript-Large and DOFA-CLIP-L-384 on the fine-grained zero-shot classification task.

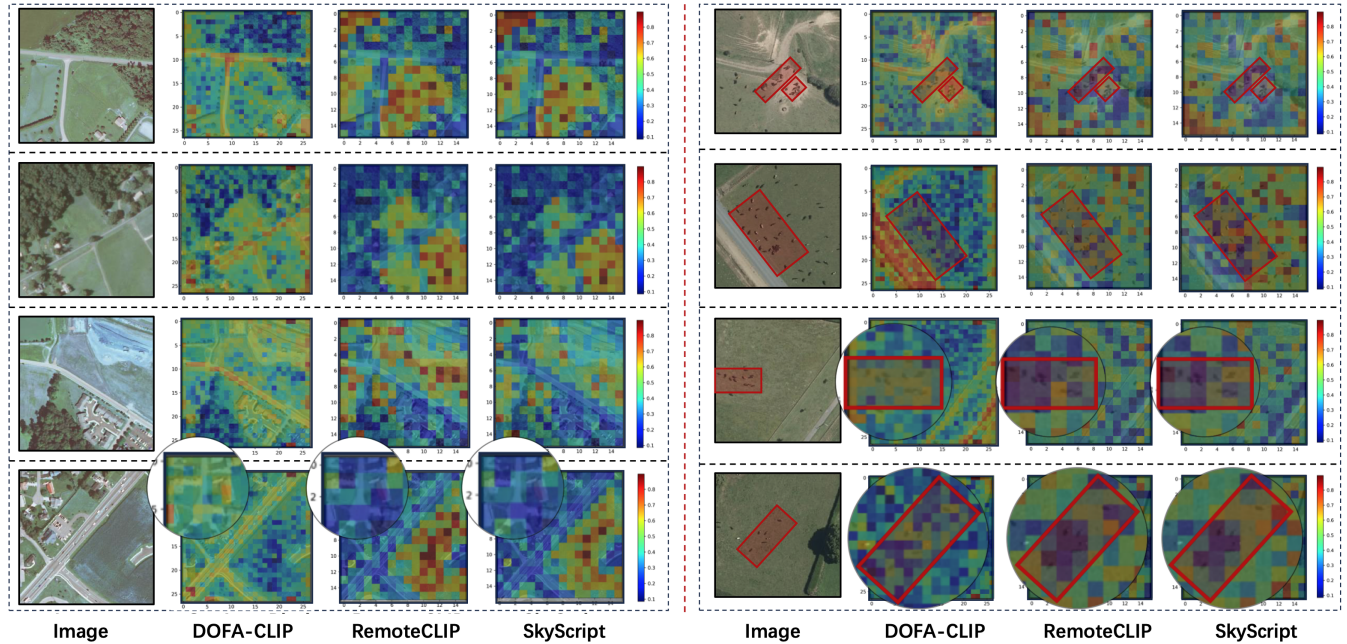


Figure 27: Visualization of features from RemoteCLIP (ViT-L), SkyScript (ViT-L), and DOFA-CLIP-L-384 on the m-chesapeake and m-nz-cattle datasets from GEO-Bench.

- Astruc, G.; Gonthier, N.; Mallet, C.; and Landrieu, L. 2024b. Omnisat: Self-supervised modality fusion for earth observation. In *European Conference on Computer Vision*, 409–427. Springer.
- Bastani, F.; Wolters, P.; Gupta, R.; Ferdinando, J.; and Kembhavi, A. 2023. Satlaspretrain: A large-scale dataset for remote sensing image understanding. In *Proceedings of the IEEE/CVF International Conference on Computer Vision*, 16772–16782.
- Bountos, N. I.; Ouaknine, A.; and Rolnick, D. 2023. FoMo-Bench: a multi-modal, multi-scale and multi-task Forest Monitoring Benchmark for remote sensing foundation models. *arXiv preprint arXiv:2312.10114*.
- Braham, N. A. A.; Albrecht, C. M.; Mairal, J.; Chanussot, J.; Wang, Y.; and Zhu, X. X. 2024. Spectralearth: Training hyperspectral foundation models at scale. *arXiv preprint arXiv:2408.08447*.
- Chen, X.; Wang, X.; Changpinyo, S.; Piergiovanni, A.; Padlewski, P.; Salz, D.; Goodman, S.; Grycner, A.; Mustafa, B.; Beyer, L.; et al. 2022. Pali: A jointly-scaled multilingual language-image model. *arXiv preprint arXiv:2209.06794*.
- Cheng, G.; Han, J.; and Lu, X. 2017. Remote sensing image scene classification: Benchmark and state of the art. *Proceedings of the IEEE*, 105(10): 1865–1883.
- Christie, G.; Fendley, N.; Wilson, J.; and Mukherjee, R. 2018. Functional map of the world. In *Proceedings of the IEEE Conference on Computer Vision and Pattern Recognition*, 6172–6180.
- Cong, Y.; Khanna, S.; Meng, C.; Liu, P.; Rozi, E.; He, Y.; Burke, M.; Lobell, D.; and Ermon, S. 2022. SatMAE: Pre-training transformers for temporal and multi-spectral satellite imagery. *Advances in Neural Information Processing Systems*, 35: 197–211.
- Dosovitskiy, A.; Beyer, L.; Kolesnikov, A.; Weissenborn, D.; Zhai, X.; Unterthiner, T.; Dehghani, M.; Minderer, M.; Heigold, G.; Gelly, S.; et al. 2020. An image is worth 16x16 words: Transformers for image recognition at scale. *arXiv preprint arXiv:2010.11929*.
- Fuller, A.; Millard, K.; and Green, J. R. 2023. CROMA: Remote sensing representations with contrastive radar-optical masked autoencoders. *arXiv preprint arXiv:2311.00566*.
- Garioud, A.; De Wit, A.; Poupée, M.; Valette, M.; Giordano, S.; and Wattrelos, B. 2023. FLAIR# 2: textural and temporal information for semantic segmentation from multi-source optical imagery. *arXiv preprint arXiv:2305.14467*.
- Girdhar, R.; El-Nouby, A.; Liu, Z.; Singh, M.; Alwala, K. V.; Joulin, A.; and Misra, I. 2023. Imagebind: One embedding space to bind them all. In *Proceedings of the IEEE/CVF conference on computer vision and pattern recognition*, 15180–15190.
- Guanter, L.; Kaufmann, H.; Segl, K.; Foerster, S.; Rogass, C.; Chabrillat, S.; Kuester, T.; Hollstein, A.; Rossner, G.; Chlebek, C.; et al. 2015. The EnMAP spaceborne imaging spectroscopy mission for Earth observation. *Remote Sensing*, 7(7): 8830–8857.
- Guo, X.; Lao, J.; Dang, B.; Zhang, Y.; Yu, L.; Ru, L.; Zhong, L.; Huang, Z.; Wu, K.; Hu, D.; et al. 2024. Skysense: A multi-modal remote sensing foundation model towards universal interpretation for earth observation imagery. In *Proceedings of the IEEE/CVF Conference on Computer Vision and Pattern Recognition*, 27672–27683.
- Helber, P.; Bischke, B.; Dengel, A.; and Borth, D. 2019. Eurosat: A novel dataset and deep learning benchmark for land use and land cover classification. *IEEE Journal of Selected Topics in Applied Earth Observations and Remote Sensing*, 12(7): 2217–2226.
- Hong, D.; Zhang, B.; Li, X.; Li, Y.; Li, C.; Yao, J.; Yokoya, N.; Li, H.; Ghamisi, P.; Jia, X.; et al. 2024. SpectralGPT: Spectral remote sensing foundation model. *IEEE Transactions on Pattern Analysis and Machine Intelligence*.
- Ilharco, G.; Wortsman, M.; Gadre, S. Y.; Song, S.; Hajsirzi, H.; Kornblith, S.; Farhadi, A.; and Schmidt, L. 2022. Patching open-vocabulary models by interpolating weights. *Advances in Neural Information Processing Systems*, 35: 29262–29277.
- Irvin, J.; Sheng, H.; Ramachandran, N.; Johnson-Yu, S.; Zhou, S.; Story, K.; Rustowicz, R.; Elsworth, C.; Austin, K.; and Ng, A. Y. 2020. Forestnet: Classifying drivers of deforestation in indonesia using deep learning on satellite imagery. *arXiv preprint arXiv:2011.05479*.
- Irvin, J. A.; Liu, E. R.; Chen, J. C.; Dormoy, I.; Kim, J.; Khanna, S.; Zheng, Z.; and Ermon, S. 2024. TeoChat: A large vision-language assistant for temporal earth observation data. *arXiv preprint arXiv:2410.06234*.
- Kikaki, K.; Kakogeorgiou, I.; Hoteit, I.; and Karantzalos, K. 2024. Detecting marine pollutants and sea surface features with deep learning in sentinel-2 imagery. *ISPRS Journal of Photogrammetry and Remote Sensing*, 210: 39–54.
- Kuckreja, K.; Danish, M. S.; Naseer, M.; Das, A.; Khan, S.; and Khan, F. S. 2024. GeoChat: Grounded large vision-language model for remote sensing. In *Proceedings of the IEEE/CVF Conference on Computer Vision and Pattern Recognition*, 27831–27840.
- Lacoste, A.; Lehmann, N.; Rodriguez, P.; Sherwin, E.; Kerner, H.; Lütjens, B.; Irvin, J.; Dao, D.; Alemohammad, H.; Drouin, A.; et al. 2024. Geo-bench: Toward foundation models for earth monitoring. *Advances in Neural Information Processing Systems*, 36.
- Li, H.; Dou, X.; Tao, C.; Hou, Z.; Chen, J.; Peng, J.; Deng, M.; and Zhao, L. 2017. RSI-CB: A large scale remote sensing image classification benchmark via crowdsourcing data. *arXiv preprint arXiv:1705.10450*.
- Li, X.; Ding, J.; and Elhoseiny, M. 2024. Vrsbench: A versatile vision-language benchmark dataset for remote sensing image understanding. *arXiv preprint arXiv:2406.12384*.
- Li, X.; Wen, C.; Hu, Y.; and Zhou, N. 2023. RS-CLIP: Zero shot remote sensing scene classification via contrastive vision-language supervision. *International Journal of Applied Earth Observation and Geoinformation*, 124: 103497.
- Liu, F.; Chen, D.; Guan, Z.; Zhou, X.; Zhu, J.; Ye, Q.; Fu, L.; and Zhou, J. 2024. Remoteclip: A vision language founda-

tion model for remote sensing. *IEEE Transactions on Geoscience and Remote Sensing*.

Liu, H.; Li, C.; Wu, Q.; and Lee, Y. J. 2023. Visual instruction tuning. *Advances in neural information processing systems*, 36: 34892–34916.

Long, Y.; Xia, G.-S.; Li, S.; Yang, W.; Yang, M. Y.; Zhu, X. X.; Zhang, L.; and Li, D. 2021. On creating benchmark dataset for aerial image interpretation: Reviews, guidances, and million-aid. *IEEE Journal of selected topics in applied earth observations and remote sensing*, 14: 4205–4230.

Mendieta, M.; Han, B.; Shi, X.; Zhu, Y.; and Chen, C. 2023. Towards geospatial foundation models via continual pre-training. In *Proceedings of the IEEE/CVF International Conference on Computer Vision*, 16806–16816.

Montello, F.; Arnaudo, E.; and Rossi, C. 2022. Mmflood: A multimodal dataset for flood delineation from satellite imagery. *IEEE Access*, 10: 96774–96787.

OpenAI. 2023. GPT-4 Technical Report. Technical report, OpenAI.

OpenStreetMap contributors. 2017. Planet dump retrieved from <https://planet.osm.org>. <https://www.openstreetmap.org>.

Oquab, M.; Darcet, T.; Moutakanni, T.; Vo, H. V.; Szafraniec, M.; Khalidov, V.; Fernandez, P.; Haziza, D.; Massa, F.; El-Nouby, A.; Howes, R.; Huang, P.-Y.; Xu, H.; Sharma, V.; Li, S.-W.; Galuba, W.; Rabbat, M.; Assran, M.; Ballas, N.; Synnaeve, G.; Misra, I.; Jegou, H.; Mairal, J.; Labatut, P.; Joulin, A.; and Bojanowski, P. 2023. DINOv2: Learning Robust Visual Features without Supervision.

Radford, A.; Kim, J. W.; Hallacy, C.; Ramesh, A.; Goh, G.; Agarwal, S.; Sastry, G.; Askell, A.; Mishkin, P.; Clark, J.; et al. 2021. Learning transferable visual models from natural language supervision. In *International conference on machine learning*, 8748–8763. PmLR.

Reed, C. J.; Gupta, R.; Li, S.; Brockman, S.; Funk, C.; Clipp, B.; Keutzer, K.; Candido, S.; Uyttendaele, M.; and Darrell, T. 2023. Scale-MAE: A scale-aware masked autoencoder for multiscale geospatial representation learning. In *Proceedings of the IEEE/CVF International Conference on Computer Vision*, 4088–4099.

Sastry, S.; Khanal, S.; Dhakal, A.; Ahmad, A.; and Jacobs, N. 2025. Taxabind: A unified embedding space for ecological applications. In *2025 IEEE/CVF Winter Conference on Applications of Computer Vision (WACV)*, 1765–1774. IEEE.

Stewart, A.; Lehmann, N.; Corley, I.; Wang, Y.; Chang, Y.-C.; Ait Ali Braham, N. A.; Sehgal, S.; Robinson, C.; and Banerjee, A. 2023. SSL4EO-L: Datasets and foundation models for Landsat imagery. *Advances in Neural Information Processing Systems*, 36: 59787–59807.

Stewart, A. J.; Robinson, C.; Corley, I. A.; Ortiz, A.; Lavista Ferres, J. M.; and Banerjee, A. 2022. TorchGeo: Deep Learning With Geospatial Data. In *Proceedings of the 30th International Conference on Advances in Geographic Information Systems, SIGSPATIAL '22*, 1–12. Seattle, Washington: Association for Computing Machinery.

Sumbul, G.; Charfuelan, M.; Demir, B.; and Markl, V. 2019. Bigearthnet: A large-scale benchmark archive for remote sensing image understanding. In *IGARSS 2019-2019 IEEE international geoscience and remote sensing symposium*, 5901–5904. IEEE.

Sun, X.; Sun, Y.; and Wang, Z. 2020. High-Resolution SAR Ship Object Detection Dataset - 2.0. Online.

Tang, M.; Cozma, A.; Georgiou, K.; and Qi, H. 2024. Cross-Scale MAE: A tale of multiscale exploitation in remote sensing. *Advances in Neural Information Processing Systems*, 36.

Vaswani, A.; Shazeer, N.; Parmar, N.; Uszkoreit, J.; Jones, L.; Gomez, A. N.; Kaiser, Ł.; and Polosukhin, I. 2017. Attention is all you need. *Advances in neural information processing systems*, 30.

Wang, D.; Hu, M.; Jin, Y.; Miao, Y.; Yang, J.; Xu, Y.; Qin, X.; Ma, J.; Sun, L.; Li, C.; et al. 2024a. Hypersigma: Hyperspectral intelligence comprehension foundation model. *arXiv preprint arXiv:2406.11519*.

Wang, Y.; Albrecht, C. M.; Braham, N. A. A.; Liu, C.; Xiong, Z.; and Zhu, X. X. 2024b. Decoupling common and unique representations for multimodal self-supervised learning. In *European Conference on Computer Vision*, 286–303. Springer.

Wang, Y.; Braham, N. A. A.; Xiong, Z.; Liu, C.; Albrecht, C. M.; and Zhu, X. X. 2023a. SSL4EO-S12: A large-scale multimodal, multitemporal dataset for self-supervised learning in Earth observation [Software and Data Sets]. *IEEE Geoscience and Remote Sensing Magazine*, 11(3): 98–106.

Wang, Y.; Hernández, H. H.; Albrecht, C. M.; and Zhu, X. X. 2023b. Feature guided masked autoencoder for self-supervised learning in remote sensing. *arXiv preprint arXiv:2310.18653*.

Wang, Z.; Prabha, R.; Huang, T.; Wu, J.; and Rajagopal, R. 2024c. Skyscript: A large and semantically diverse vision-language dataset for remote sensing. In *Proceedings of the AAAI Conference on Artificial Intelligence*, volume 38, 5805–5813.

Wei, S.; Zeng, X.; Qu, Q.; Wang, M.; Su, H.; and Shi, J. 2020. HRSID: A high-resolution SAR images dataset for ship detection and instance segmentation. *Ieee Access*, 8: 120234–120254.

Weinstein, B. G.; Graves, S. J.; Marconi, S.; Singh, A.; Zare, A.; Stewart, D.; Bohlman, S. A.; and White, E. P. 2021. A benchmark dataset for canopy crown detection and delineation in co-registered airborne RGB, LiDAR and hyperspectral imagery from the National Ecological Observation Network. *PLoS computational biology*, 17(7): e1009180.

Xia, G.-S.; Bai, X.; Ding, J.; Zhu, Z.; Belongie, S.; Luo, J.; Datcu, M.; Pelillo, M.; and Zhang, L. 2018. DOTA: A large-scale dataset for object detection in aerial images. In *Proceedings of the IEEE conference on computer vision and pattern recognition*, 3974–3983.

Xia, G.-S.; Hu, J.; Hu, F.; Shi, B.; Bai, X.; Zhong, Y.; Zhang, L.; and Lu, X. 2017. AID: A benchmark data set for performance evaluation of aerial scene classification. *IEEE Trans-*

- actions on Geoscience and Remote Sensing*, 55(7): 3965–3981.
- Xiong, Z.; Wang, Y.; Zhang, F.; Stewart, A. J.; Hanna, J.; Borth, D.; Papoutsis, I.; Le Saux, B.; Camps-Valls, G.; and Zhu, X. X. 2024a. Neural plasticity-inspired foundation model for observing the Earth crossing modalities. *arXiv e-prints*, arXiv-2403.
- Xiong, Z.; Wang, Y.; Zhang, F.; and Zhu, X. X. 2024b. One for all: Toward unified foundation models for Earth vision. *arXiv preprint arXiv:2401.07527*.
- Xiong, Z.; Zhang, F.; Wang, Y.; Shi, Y.; and Zhu, X. X. 2024c. EarthNets: Empowering artificial intelligence for Earth observation. *IEEE Geoscience and Remote Sensing Magazine*.
- Yuan, Z.; Xiong, Z.; Mou, L.; and Zhu, X. X. 2024. Chatearthnet: A global-scale image-text dataset empowering vision-language geo-foundation models. *Earth System Science Data Discussions*, 2024: 1–24.
- Yuan, Z.; Zhang, W.; Fu, K.; Li, X.; Deng, C.; Wang, H.; and Sun, X. 2022a. Exploring a fine-grained multiscale method for cross-modal remote sensing image retrieval. *arXiv preprint arXiv:2204.09868*.
- Yuan, Z.; Zhang, W.; Rong, X.; Li, X.; Chen, J.; Wang, H.; Fu, K.; and Sun, X. 2021. A lightweight multi-scale cross-modal text-image retrieval method in remote sensing. *IEEE Transactions on Geoscience and Remote Sensing*, 60: 1–19.
- Yuan, Z.; Zhang, W.; Tian, C.; Rong, X.; Zhang, Z.; Wang, H.; Fu, K.; and Sun, X. 2022b. Remote sensing cross-modal text-image retrieval based on global and local information. *IEEE Transactions on Geoscience and Remote Sensing*, 60: 1–16.
- Zhai, X.; Mustafa, B.; Kolesnikov, A.; and Beyer, L. 2023. Sigmoid loss for language image pre-training. In *Proceedings of the IEEE/CVF international conference on computer vision*, 11975–11986.
- Zhan, Y.; Xiong, Z.; and Yuan, Y. 2025. Skyeyegpt: Unifying remote sensing vision-language tasks via instruction tuning with large language model. *ISPRS Journal of Photogrammetry and Remote Sensing*, 221: 64–77.
- Zhang, T.; Zhang, X.; Li, J.; Xu, X.; Wang, B.; Zhan, X.; Xu, Y.; Ke, X.; Zeng, T.; Su, H.; et al. 2021. SAR ship detection dataset (SSDD): Official release and comprehensive data analysis. *Remote Sensing*, 13(18): 3690.
- Zhang, W.; Cai, M.; Zhang, T.; Zhuang, Y.; and Mao, X. 2024a. Earthgpt: A universal multi-modal large language model for multi-sensor image comprehension in remote sensing domain. *IEEE Transactions on Geoscience and Remote Sensing*.
- Zhang, Z.; Zhao, T.; Guo, Y.; and Yin, J. 2024b. RS5M and GeoRSCLIP: A large scale vision-language dataset and a large vision-language model for remote sensing. *IEEE Transactions on Geoscience and Remote Sensing*.
- Zhou, W.; Newsam, S.; Li, C.; and Shao, Z. 2018. PatternNet: A benchmark dataset for performance evaluation of remote sensing image retrieval. *ISPRS journal of photogrammetry and remote sensing*, 145: 197–209.
- Zhu, B.; Lin, B.; Ning, M.; Yan, Y.; Cui, J.; Wang, H.; Pang, Y.; Jiang, W.; Zhang, J.; Li, Z.; et al. 2023. Language-bind: Extending video-language pretraining to n-modality by language-based semantic alignment. *arXiv preprint arXiv:2310.01852*.
- Zhu, X. X.; Hu, J.; Qiu, C.; Shi, Y.; Kang, J.; Mou, L.; Bagheri, H.; Häberle, M.; Hua, Y.; Huang, R.; et al. 2019. So2Sat LCZ42: A benchmark dataset for global local climate zones classification. *arXiv preprint arXiv:1912.12171*.
- Zhu, X. X.; Tuia, D.; Mou, L.; Xia, G.-S.; Zhang, L.; Xu, F.; and Fraundorfer, F. 2017. Deep learning in remote sensing: A comprehensive review and list of resources. *IEEE geoscience and remote sensing magazine*, 5(4): 8–36.
- Zhu, X. X.; Xiong, Z.; Wang, Y.; Stewart, A. J.; Heidler, K.; Wang, Y.; Yuan, Z.; Dujardin, T.; Xu, Q.; and Shi, Y. 2024. On the foundations of earth and climate foundation models. *arXiv preprint arXiv:2405.04285*.